RSC Advances

PAPER

View Article Online
View Journal | View Issue

Cite this: *RSC Adv.*, 2023, **13**, 31820

Alkali metal doped crystalline g-C_3N_4 with an enriched cyano group for visible-light photocatalytic degradation of methylamine†

Peiyao Xiong,[ab] Qian Li,[abc] Qijun Tang,[ab] Haiqiang Wang *[ab] and Zhongbiao Wu *[ab]

Received 6th September 2023
Accepted 21st October 2023

DOI: 10.1039/d3ra06066g

rsc.li/rsc-advances

In this study, alkali-metal-doped crystalline g-C_3N_4 with an enriched cyano group was synthesized using the molten salt method and used for the visible-light photocatalytic degradation of methylamine (MA), a common organic amine compound with a low odor threshold. Different types and proportions of melting salts (Li, K, and Na) were added during secondary calcination to regulate the morphology, crystallinity, and surface defects of graphitic carbon nitride (g-C_3N_4). With molten salt treatment matched the melting point of the binary salt system, a cyano group and alkali metal co-doped crystalline g-C_3N_4 with a high surface area and good crystallinity were prepared. Co-decorating the alkali metal and cyano groups on crystalline g-C_3N_4 facilitated the adsorption of MA, realized an excellent photo-charge transfer efficiency, and generated more superoxide radicals. Compared with pristine g-C_3N_4 (PCN), the apparent rate constant of LiK15 : 5-CCN for the degradation of MA increased by 10.2 times and the degradation efficiency of 1000 ppm MA gas was 93.1% after 90 min of irradiation with visible light, whereas the degradation efficiency of PCN was 19.2%.

1. Introduction

Methylamine (MA) is a common organic amine that is widely used or generated in various industrial and agricultural activities. Methylamine is very odorous; it has a low odor threshold and a strong fishy odor.[1,2] The odor problems caused by the emission of MA have led to social issues, negative impacts on human health, local economies, and have consequently attracted much attention.[3–5]

To solve the malodor problem, physical and chemical methods have been widely used.[6–9] However, the low degradation efficiency, economic cost, and disposal of wasted sorbents or absorbents hinder further applications, including thermal catalytic degradation, adsorption, and wet scrubbers. Therefore, the development of advanced and economic technologies to cope with odors remains a significant challenge.

Photocatalytic degradation is an effective and economical way to eliminate atmospheric gaseous contaminants, including NH_3, H_2S, and MA.[10–12] Kachina[13] *et al.* studied the reaction pathway and products of the photocatalytic oxidation (PCO) of MA on titanium dioxide in aqueous and gas phases. A high MA degradation efficiency was achieved, and no deactivation of the TiO_2 catalyst was observed. Helali[14] *et al.* investigated the influence of various parameters, including concentration, irradiation time, pH, UV domain, and UV-A/UV-B radiant fluxes, on photocatalytic degradation of MA and found that UV-B was more efficient than UV-A for the elimination of MA. Furthermore, malodorous gases were mainly generated in buildings or man-made structures; consequently, UV-B light causing minimal harm to humans, or visible light are suitable light sources for the photocatalytic degradation of MA.

Graphitic carbon nitride (g-C_3N_4) with a highly conjugated π system composed of basic structural units of triazine (C_3N_3) and heptazine (C_6N_7) rings was a suitable candidate for the purpose of MA elimination using UV-B or visible light.[15] It has a suitable bandgap of ~2.7 eV, which can absorb visible light, and it also has the advantages of being environmentally friendly, easily prepared, and physically and chemically stable. However, pristine g-C_3N_4 (PCN) with layered bulk structures fails to meet the demand for high photocatalytic efficiency because it exhibits weak visible light absorbance, insufficient surface reaction sites, high mass transfer resistance, and rapid charge carrier recombination.[16,17]

[a]*Key Laboratory of Environment Remediation and Ecological Health, Ministry of Education, College of Environmental & Resources Science, Zhejiang University, Hangzhou, 310058, P. R. China. E-mail: haiqiangwang@zju.edu.cn; zbwu@zju.edu.cn; Fax: +86-571-87073074; Tel: +86-571-87073074*

[b]*Zhejiang Tianlan Environmental Protection Technology Co., Ltd, Zhejiang Provincial Engineering Research Center of Industrial Boiler & Furnace Flue Gas Pollution Control, Hangzhou, 311202, P. R. China*

[c]*Department of Environmental Science and Engineering, School of Petrochemical Engineering & Environment, Zhejiang Ocean University, Zhoushan, 316022, P. R. China*

† Electronic supplementary information (ESI) available. See DOI: https://doi.org/10.1039/d3ra06066g

To enhance the photocatalytic activity of PCN, several material modification and defect decoration strategies have been developed, including metal and non-metal doping,[18,19] heterostructure construction,[20–23] morphological control,[24,25] crystallinity regulation[26–29] and defect modulation.[30–33] Among these, the use of a molten salt enhances crystallinity and produces highly crystalline g-C_3N_4 (CCN).[34,35] The higher crystallinity and surface groups in CCN help reduce electron–hole recombination and accelerate charge transfer. Currently, significant interest has been devoted to the introduction of cyano groups and alkali metal ions during molten salt treatment. Metal-ion-assisted methods can simultaneously induce cyano defects as proton acceptors and metal ion dopants as hole donors in the CN framework.[36] Cyano groups can adjust the electronic structure, promote charge mobility on the surface of g-C_3N_4 and serve as chemisorption sites for reactants.[37] Furthermore, the doping of alkali metal ions can establish ion–dipole interactions with nitrogen tanks in CN to optimize energy band and electronic structures.

This study synthesized alkali metal doped crystalline g-C_3N_4 with enriched cyano group using a molten salt method to generate high MA degradation efficiency under visible light irradiation. Different mixed melts (LiCl–KCl–NaCl) with different ratios were selected to regulate the surface groups, alkali metal ions, and crystallization of CCN. The physicochemical properties of different types of CCN and their photocatalytic degradation performances under visible-light irradiation were systematically analyzed and compared. We hope that this work will provide new insights into the potential applications of crystalline g-C_3N_4 photocatalysts for malodorous photocatalytic elimination.

2. Experimental

2.1 Materials and chemicals

Urea ($CO(NH_2)_2$) was purchased from Shanghai Aladdin Chemistry Technology Co., Ltd. Lithium chloride (LiCl), sodium chloride (NaCl), potassium chloride (KCl) and ethanol (C_2H_5OH, 75%) were purchased from Sinopharm Chemical Reagent Co., Ltd. All chemicals were used without further purification.

2.2 Sample synthesis

2.2.1 Preparation of pristine g-C_3N_4. The preparation of PCN was carried out by heating 20.0 g of urea in a 100 mL crucible in the muffle furnace. The heating was conducted at a rate of 10 °C min^{-1} from room temperature to 550 °C and was stabilized for 2 hours. The resulting yellowish powders were collected after natural cooling of the furnace. To minimize systematic errors, samples from different batches were mixed before use.

2.2.2 Preparation of high crystalline C_3N_4. The synthesis method was adapted from which described by Zhang[34] *et al.* with minor modifications and the preparation process was illustrated in Scheme 1. 400 mg of CN precursor was treated with a eutectic mixture of 1.8 g LiCl, 2.2 g KCl and 1 mL ethanol in a mortar for 10 minutes. The mixture was then transferred to a quartz boat and heated in a nitrogen atmosphere in a tube furnace, with the temperature ramping from 30 °C to 550 °C at a rate of 10 °C min^{-1} and held at 550 °C for 2 hours. After cooling down, the sample was washed with boiling water and dried in a vacuum oven at 60 °C, and the resulting sample was denoted as LiK–CCN (9 : 11). A series of samples were obtained by adjusting the type and mass ratio of the molten salts. In the abbreviation expression, the "CCN" designation was omitted and samples were denoted as MM(*X*), where MM represent the alkali metals using in the preparation method and *X* represents the mass ratio of chloride salts (*e.g.*, LiK3 : 17, LiK9 : 11, LiK15 : 5, NaK3 : 17, NaK9 : 11, NaK15 : 5, LiNa10 : 10, LiNa13 : 7, LiNa16 : 4).

Melting points varied with the change of mass ratio of LiCl–KCl/LiCl–NaCl and the melting point of binary eutectic chloride salts were listed in Table 1. LiK9 : 11 and LiNa13 : 7 had lowest melting point (347 °C and 546 °C) in their given systems, respectively.

2.3 Characterization

The crystal structures of as-prepared samples were determined by X-ray powder diffraction (XRD, Ultima IV, Rigaku, Japan) in a 2θ range of 5–80°. Fourier transform infrared (FTIR, Nicolet iS20, Thermo Scientific, America) was used to characterize the functional groups of samples, and the microstructures were observed by scanning electron microscopy (SEM, SU-8010, Hitachi, Japan) and transmission electron microscopy (TEM, H-9500, Hitachi, Japan). The elemental states of the samples were characterized by X-ray photoelectron spectroscopy (XPS, ESCALAB250Xi, Thermo, USA). The specific surface area and pore size distribution information of the samples were obtained by nitrogen adsorption (JW-BK132F, JEOL, Beijing). The ultraviolet-visible diffuse reflectance spectrum (UV-vis, UV-2600, SHIMADZU, Japan) of the samples were obtained using an integral sphere attachment ISR-2600. The photoluminescence spectrum (PL, FLS980, Edinburgh Instruments, England) were obtained by exciting at 325 nm wavelength at room temperature. The photocurrent–time curve, electrochemical impedance spectroscopy (EIS) and Mott–Schottky (MS) curve were tested on an electrochemical workstation (CHI660E, Chenhua Instrument, China). Methylamine temperature programmed desorption (MA-TPD) was performed on TP-5079 (Xianquan Instrument, China). Approximately 0.1 g of 40–60 mesh sample was packed into a reaction tube. After pretreating with a He gas flow rate of 30 mL min^{-1} at 100 °C for 1 h, the catalysts were saturated with 2000 ppm CH_3NH_2 (30 mL min^{-1}) at 50 °C. Following adsorption saturation, He gas (30 mL min^{-1}) was employed to purge the sample for an additional 60 minutes. TPD was then conducted at a heating rate of 10 °C min^{-1} up to 600 °C, with a mass spectrometer detecting the components in the exhaust gas. The methylamine adsorption breakthrough test of as-made catalysts was carried out on a fixed bed reactor. 0.1 g of the synthesized catalyst was weighed and coated onto 70 g glass balls with a diameter of 3 mm with the aid of anhydrous ethanol, then dried in an oven at 65 °C. The glass balls coated with the catalyst was then placed inside

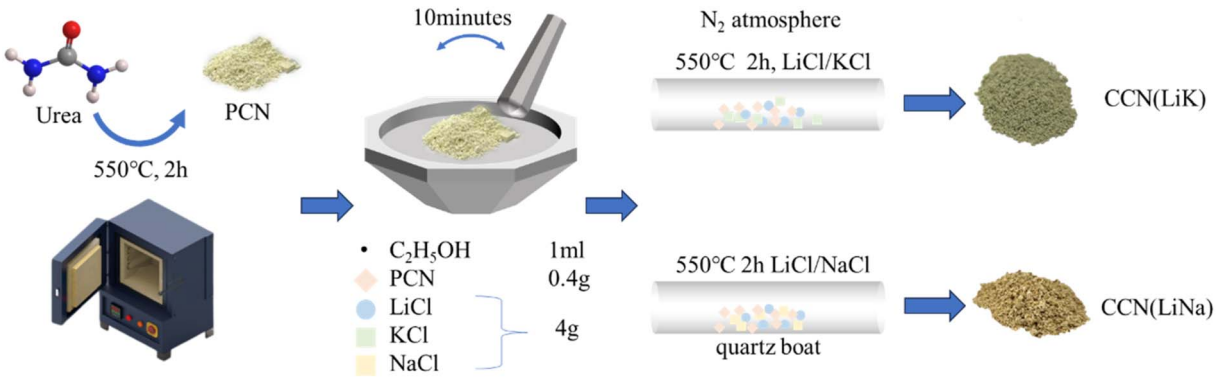

Scheme 1 Schematic diagram of synthesis of PCN & CCN.

Table 1 Melting point of binary eutectic chloride salts in a given mass ratio[38]

Alkali metals	Mass ratio (M/M)	Mole ratio	Melting point/°C
LiK	3 : 17	0.24	663
LiK	9 : 11	0.59	347
LiK	15 : 5	0.84	537
LiNa	10 : 10	0.73	568
LiNa	13 : 7	0.39	546
LiNa	16 : 4	0.18	587

the fixed bed reactor. A gas flow of 200 mL min^{-1}, containing 2000 ppm methylamine with the balance air, was injected into the reactor under the ambient condition. *In situ* diffuse reflectance FT-IR spectroscopy (*in situ* DRIFTS) was performed on Nicolet 6700 spectrometer with a spectral resolution of 4 cm^{-1}. The electron paramagnetic resonance (EPR) signals were examined on Bruker EMX plus spectrometer.

2.4 Photocatalytic performance evaluation

Methylamine photocatalytic degradation experiment was performed using a batched reactor. The reactor with a volume of

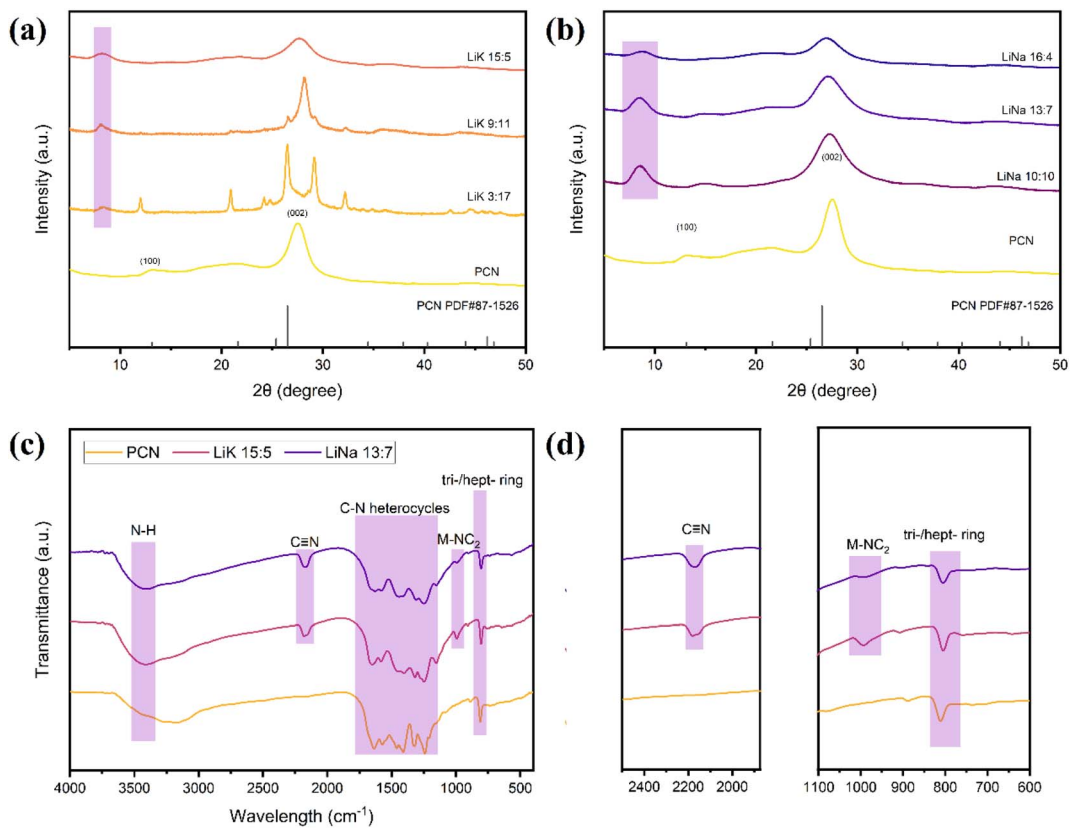

Fig. 1 (a and b) XRD and (c and d) FTIR patterns of PCN and molten salts treated CCN samples.

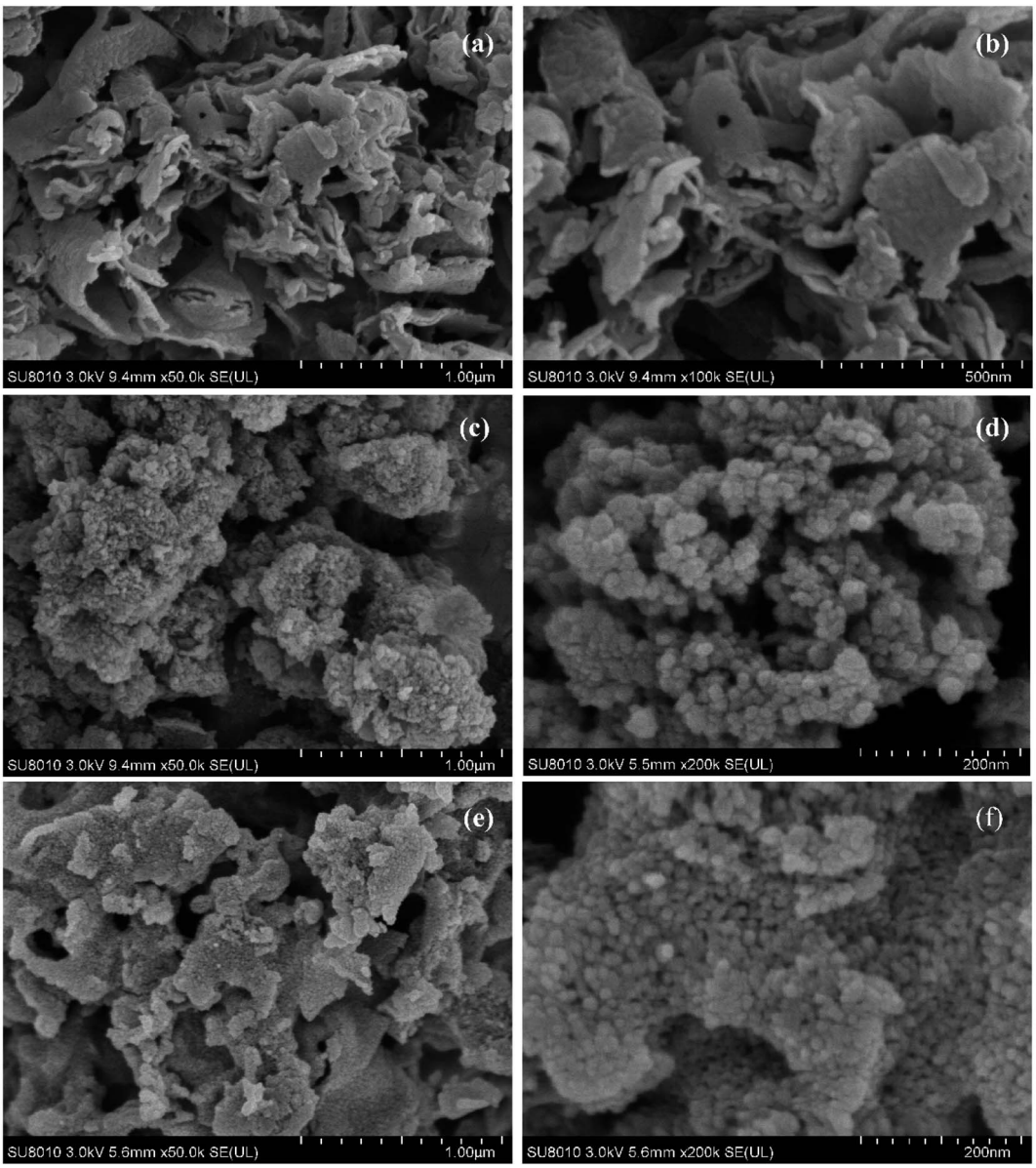

Fig. 2 Typical SEM images of (a and b) PCN, (c and d) LiK15 : 5, and (e and f) LiNa13 : 7.

2.5 liters was constructed by quartz glass. The interlayer of the reactor was maintained at a constant temperature of 25 °C by circulating water to ensure temperature stability during the reaction. A visible light filter with a cutoff wavelength of 420 nm or greater, and a 500 W xenon lamp (CEL-WLAX500, Beijing Zhongjiao Jinyuan Technology Co. Ltd, China) were placed above the reactor to allow for selective entry of visible light into the reactor.

0.1 g of the synthesized catalyst was weighed and coated onto a circular glass dish with a diameter of 10.0 cm with the aid of anhydrous ethanol, then dried in an oven at 65 °C. The glass dish coated with the catalyst was then placed inside the sealed reactor. A specific volume of saturated methylamine gas at 40 °C was aspirated using a 10 mL syringe and injected into the reactor through the inlet port. The adsorption of methylamine on the catalyst surface reached equilibrium after 30 minutes in a dark environment. Gas samples with a volume of 500 μL were fetched at interval and determined by the NPD chromatography. The photocatalytic activity measurement was initiated by turning on the xenon lamp light source after determining the initial concentration.

The visible light degradation rate of MA was calculated based on following equation:

$$\text{MA degradation } (\%) = \frac{[\text{MA}]_0 - [\text{MA}]_t}{[\text{MA}]_0} \times 100\% \quad (1)$$

where $[\text{MA}]_t$ is the concentration of methylamine at moment t, $[\text{MA}]_0$ is the initial concentration of methylamine.

Since the degradation of methylamine on the surface of the photocatalyst follows a pseudo-first-order reaction, the relationship between concentration and reaction time can be described by eqn (2).[39] Plotting the data and fitting the curve

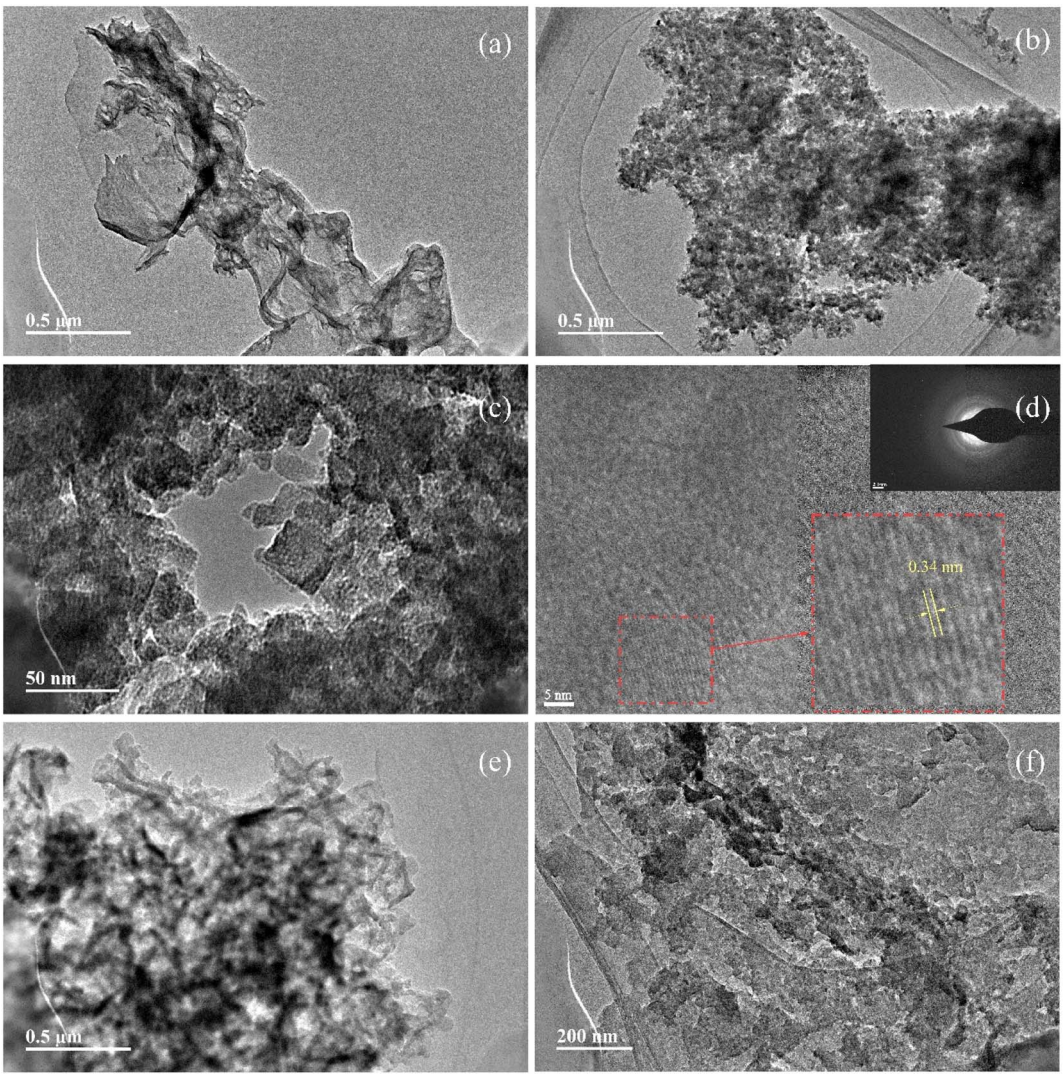

Fig. 3 Typical TEM images of (a) PCN, (b–d) LiK15 : 5, and (e and f) LiNa13 : 7. Inset in (d) is the SAED image and enlarged lattice stripe diagram.

Table 2 BET surface area of prepared CCN samples and PCN

Samples	Surface area ($m^2\ g^{-1}$)	Pore volume ($cm^3\ g^{-1}$)	Pore size (nm)
g-C_3N_4	55.6	0.43	22.90
LiK9 : 11	31.5	0.35	30.90
LiK15 : 5	85.8	0.28	10.6
LiNa10 : 10	35.2	0.10	7.17
LiNa13 : 7	51.7	0.18	11.36
LiNa16 : 4	23.1	0.12	31.8

allows determination of the rate constant for the degradation reaction of methylamine.

$$k_{obs} = \frac{\ln \frac{[MA]_0}{[MA]_t}}{t} \quad (2)$$

where k_{obs} is the reaction rate constant of methylamine.

3. Results and discussion

3.1 Physicochemical properties

All samples had a structure similar to that of PCN (Fig. 1). The two typical peaks of PCN were at 27.5° (002) and 13.2° (100), which correspond to planar stacking of the heptazine unit and aromatic ring, respectively.[40] The crystalline structures of CCN changed significantly after molten salt treatment, and there were clear differences in these changes between different treatments. Fig. 1(a) shows the XRD patterns of CCN treated with different ratios of LiCl and KCl. The XRD pattern of LiK3 : 17 is identical to that of poly(triazine imide) (PTI),[41] which is inactive for visible photocatalytic applications[42] owing to its rock-salt + salt-liquid state in the molten salt treatment.[38] As the amount of Li increased, the melting point of the binary salts decreased, and the PTI content also decreased. Small PTI peaks appeared in LiK9 : 11, and a few were observed in LiK15 : 5. The (002) peak of LiK9 : 11 showed a sharp peak and little movement to a higher angle, implying a narrower interlayer spacing.[24,34]

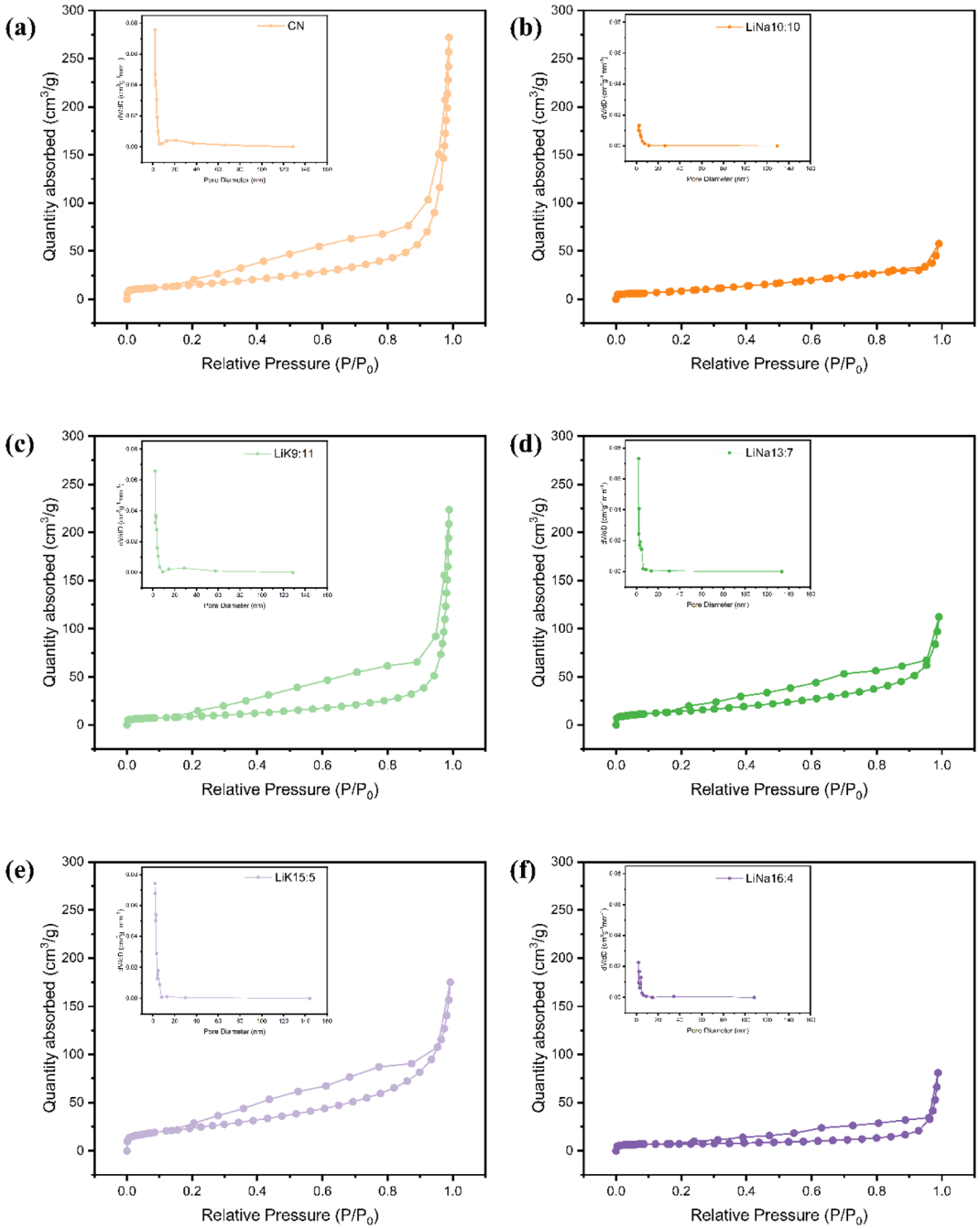

Fig. 4 Nitrogen absorption and desorption curves and BJH pore size distribution curves of PCN and CCN, (a) CN, (b) LiNa10 : 10, (c) LiK9 : 11, (d) LiNa13 : 7, (e) LiK15 : 5 and (f) LiNa16 : 4.

LiK15 : 5 showed a broader (002) peak compared to PCN, indicating that the rich defects lower the interlayer periodic ordering.[31] The (100) peak of LiKs shifted to a lower angle of 8.2°, indicating the integration of K^+ and Li^+ between the heterocyclic units.[43] In Fig. 1(b), the intensities of the (002) peaks became weaker, and the peaks broadened with an increased amount of Li, suggesting the presence of a cyano group on the surface of g-C_3N_4 and an increased number of intermediate voids.[36] Furthermore, the (100) peaks of LiNas shifted to 8.8°, which is attributed to the introduction of Na^+ and Li^+. Fig. 1(c) and (d) show the chemical structures of PCN, LiK15 : 5, and LiNa13 : 7 obtained by Fourier transform infrared (FTIR) spectroscopy. All samples exhibited a typical CN spectrum. The 810 cm^{-1} peak corresponds to the characteristic vibrational peaks of the triazine (C_3N_3) and heptazine (C_6N_7) ring units,[44] the typical 1200–1700 cm^{-1} peak could be attributed to the CN heterocycles, the N–H group represented by the broad peak between 3000 and 3400 cm^{-1} and the deformation peak at 885 cm^{-1}.[45,46] In particular, new peaks centered at 991 cm^{-1} and 2177 cm^{-1} were assigned to the interaction of

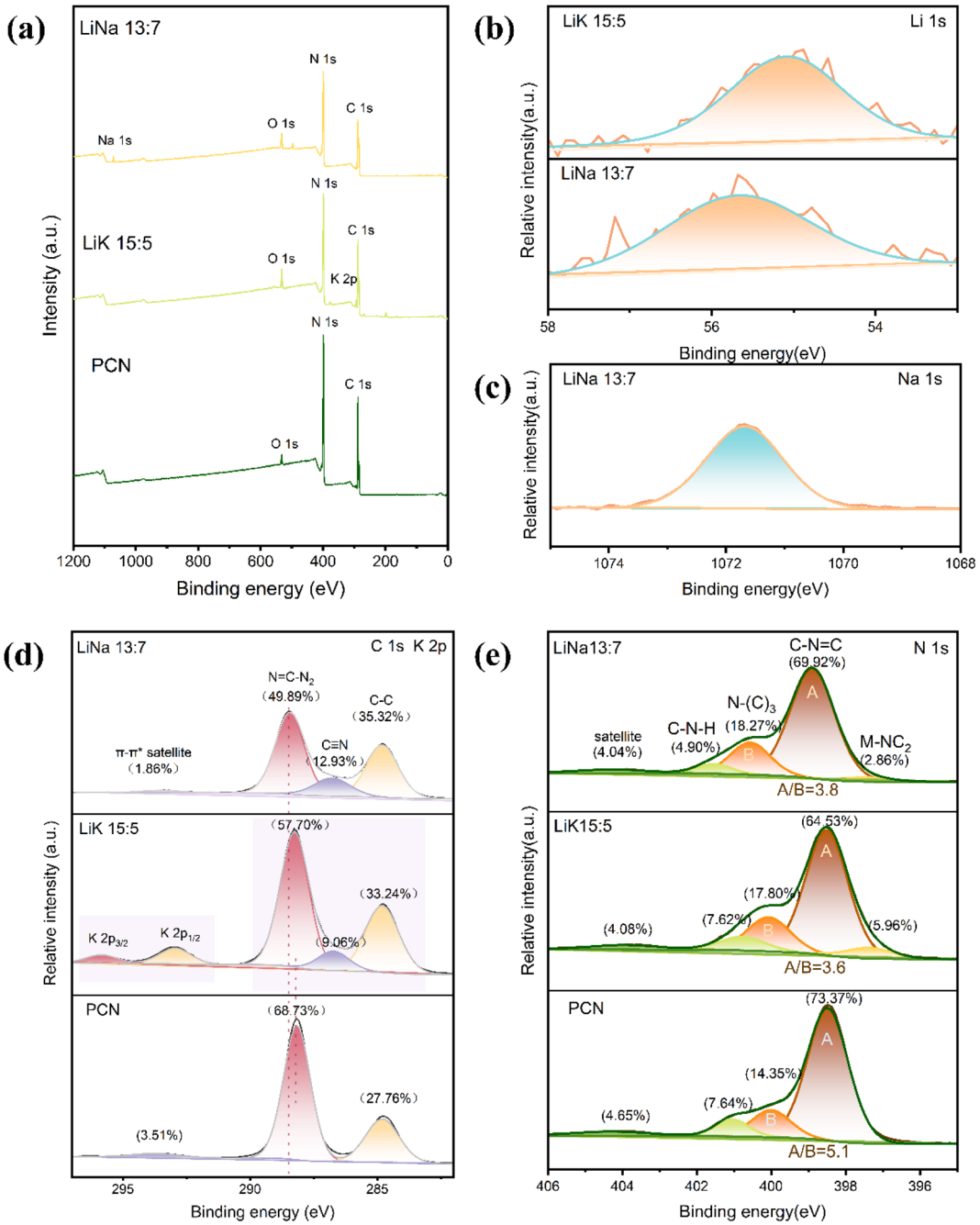

Fig. 5 (a) XPS survey, (b) high-resolution XPS Li 1s, (c) high-resolution XPS Na 1s, (d) high-resolution XPS C 1s, and (e) high-resolution XPS N 1s spectrum of PCN, LiK15 : 5, NaK15 : 5 and LiNa13 : 7.

metal–CN_2 [31] and the stretching vibration of the terminal cyano groups,[47] which revealed the introduction of alkali ions and the loss of ammonia on the surface.

Both PCN and CCN have layered structures (Fig. 2). After treatment with molten LiK salt, the surface of the layered PCN exhibited rod-like structures, with sizes of several tens of nanometers. However, the morphological change of CN treated with melted LiNa salt was not as significant as that of LiK, although it also exhibited small nanostructures. The surface of CN treated with molten LiK underwent significant changes, with a clear crystalline morphology (Fig. 3). From the selected area electron diffraction (SAED) patterns, crystal lattice stripes and diffraction rings were observed in LiK15 : 5 sample.

The Brunauer–Emmett–Teller (BET) specific area (S_{BET}), pore size, and pore volume were calculated, and are summarized in Table 2. Notably, the S_{BET} values of LiK15 : 5 (85.8 $m^2\ g^{-1}$) exceeded all others, being about 1.5 times that of PCN. The S_{BET} of LiNa13 : 7 (51.7 $m^2\ g^{-1}$) showed little change compared with that of PCN. The S_{BET} of the remaining samples decreased after treatment with molten salt. Nitrogen adsorption–desorption

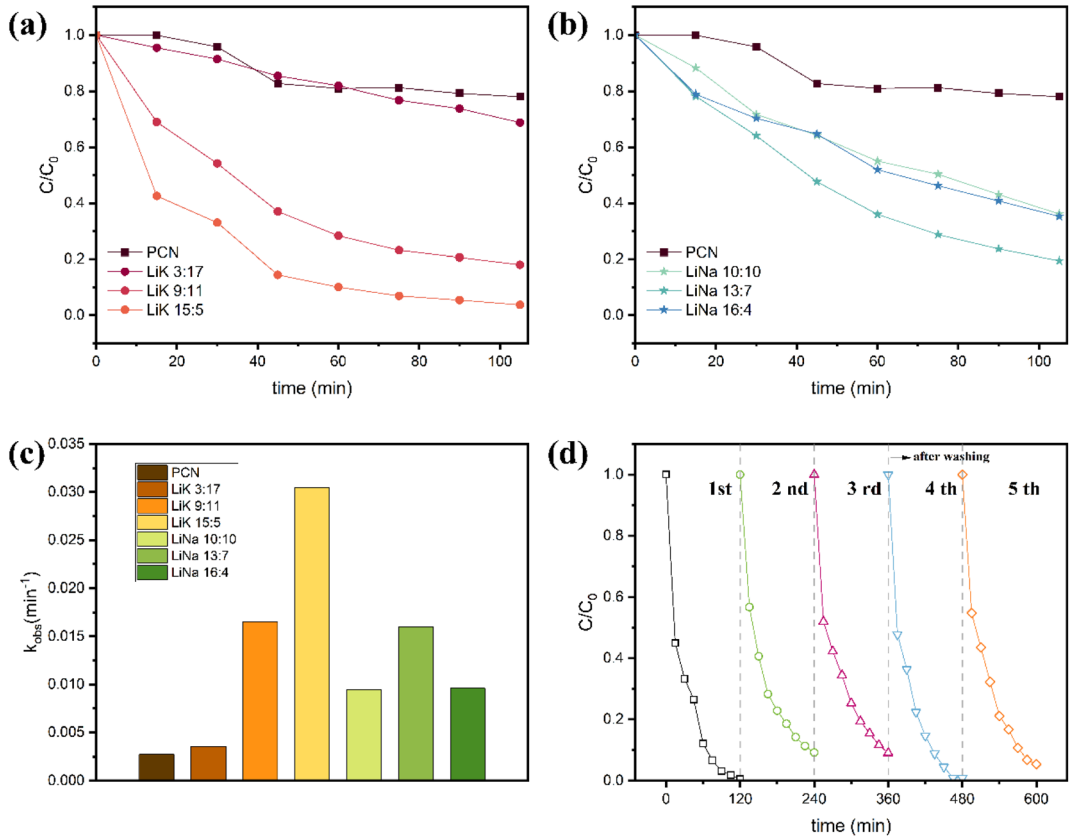

Fig. 6 (a and b) Photocatalytic degradation performances of methylamine, (c) the fitted apparent rate constants of as-prepared PCN and alkali metal doped CCN, and (d) results of repeated and recycling tests of LiK15 : 5.

isotherms and pore size distribution curves of PCN and prepared CCN samples are shown in Fig. 4. All isotherms presented typical H3-hysteresis loops[48] from 0.4 to 1.0 P/P_0, confirming the existence of micropores. The hysteresis loops of all the composites were wider than those of pure g-C_3N_4, indicating the formation of more lattice defects or micropores. In particular, the melting point of the two samples (LiK15 : 5 and LiNa13 : 7) with larger surface areas were the closest to the treatment temperature, indicating that the melting point was suitable for recrystallization and structure reconstruction of CCN.

The elemental composition of PCN is C, N, and O, and the sample treated with alkali metal ions contained additional elements, including Li, Na, and K (Fig. 5(a)). Samples treated with LiK and LiNa all showed the presence of Li, K, and Na (Fig. 5(b and c)). These results indicate that small amounts of Li, K, and Na were doped into PCN during the secondary sintering process. Fig. 5(d) shows the high-resolution XPS C 1s spectrum of the samples. The three peaks of C 1s peaks located at 284.8 eV, 286.6 eV, and 288.1 eV corresponded to the C–C single bond, C≡N, and N=C–N_2, respectively. The apparent C≡N peaks in CCN samples implied that the melting salt treatment not only retained the core structure of CN but also introduced rich cyano groups at the terminal of framework, in agreement with the FT-IR results.[31] The N 1s spectrum in Fig. 5(e) shows that PCN has roughly three peaks. The peaks at 398.5 and 400.0 eV correspond to the N atoms on the heptazine ring (C–N=C) and N–$(C)_3$, respectively, whereas the peak at 401.1 eV was related to the bridging N.[49] For CCN samples, a new N 1s peak at 397.5 eV in M–NC_2 attributed to M–N species confirmed that the CCN layers were coordinated by M–N bonds, in accordance with the results of XRD and FT-IR spectra.[31] The C–N–H peaks in CCN diminished significantly, indicating extended condensation compared to PCN. Compared to PCN, the proportions of the N–$(C)_3$ peaks of LiK15 : 5 and LiNa13 : 7 increased, indicating an increase in the proportion of heptazine rings.[34]

3.2 Methylamine photocatalytic degradation performance

The efficiency of methylamine photocatalytic degradation of various samples under visible-light irradiation were compared and are presented in Fig. 6(a)–(d). Fig. 6(a) shows that PCN displays relatively poor methylamine degradation, with a removal efficiency of only 19.2% after 2 h of reaction. LiK3 : 17 also exhibited a low rate of degradation, but the best-performing sample, LiK15 : 5, demonstrated a 10.2-fold increase in the apparent rate constant compared to the initial CN (Fig. 6(c)). During 90 min of illumination from a >420 nm xenon lamp, LiK15 : 5 showed a 93.1% rate of degradation of 1000 ppm methylamine gas, significantly outperforming the 19.2% degradation rate of PCN. For the LiK molten salt series, the melting points of LiK3 : 17, LiK9 : 11 and LiK15 : 5 were 663 °

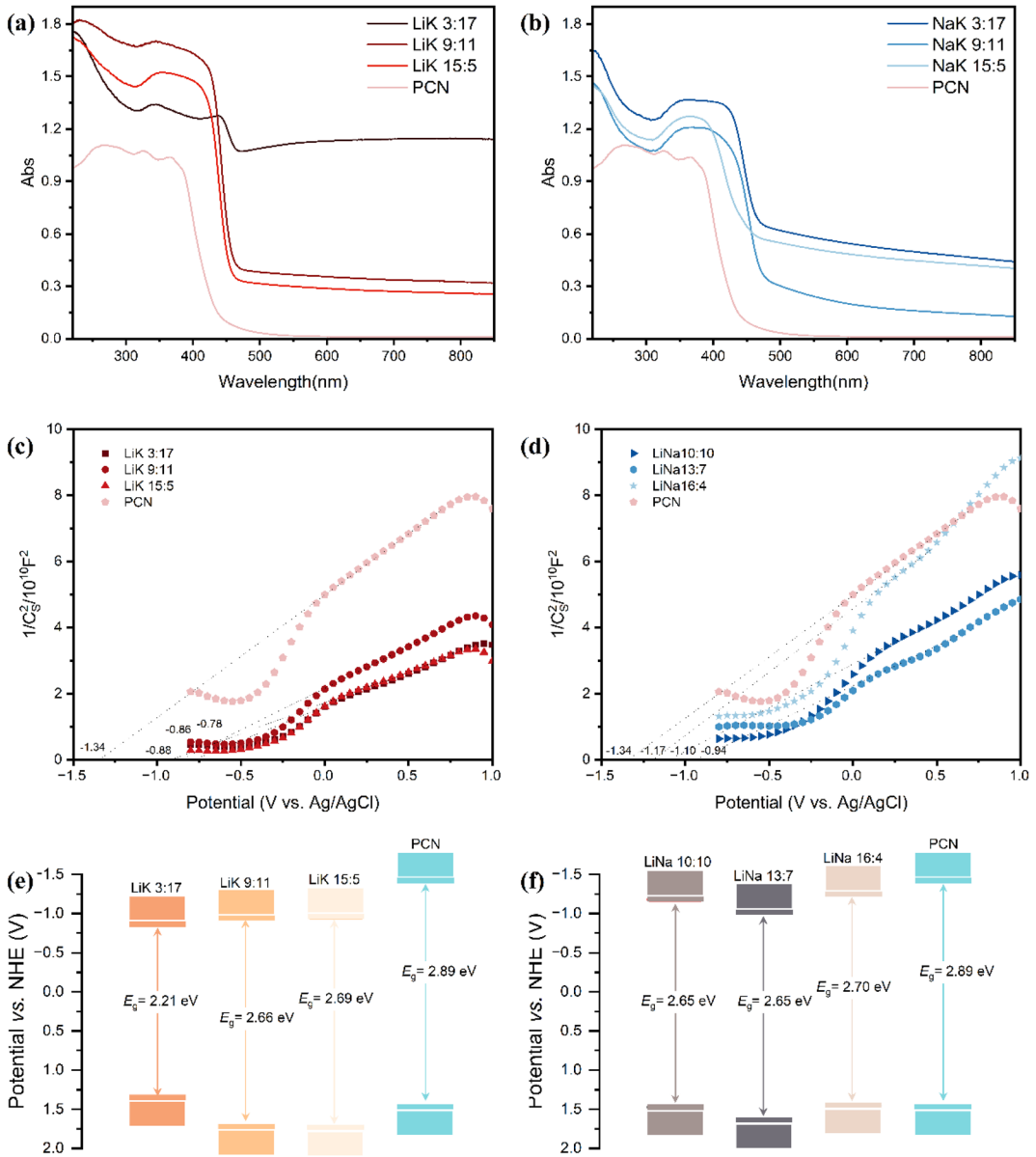

Fig. 7 (a and b) UV-vis, (c and d) Mott–Schottky plots, and (e and f) schematic diagram of the bandgap of PCN and alkali metal doped CCN.

C, 347 °C and 537 °C, respectively. The photocatalytic activity sequence of the LiK molten salt series was ranked as follows: LiK15 : 5 > LiK9 : 11 > LiK3 : 17, which accorded with the matching degree of treatment temperature and melting point of the binary salt. Fig. 6(b) shows the methylamine degradation activity of the LiNa sample. LiNa13 : 7 showed a 4.9-fold increase compared to that of PCN. The melting points of LiNa10 : 10, LiNa13 : 7 and LiNa16 : 4 were 568 °C, 546 °C, and 587 °C, respectively. Additionally, the cycle stability of LiK15 : 5 photocatalytic methylamine degradation showed that the activity of methylamine degradation remained above 90% after five cycles of experiments, while the degradation rate slightly declined in the first three consecutive tests, but then recovered the initial activity after water washing (Fig. 6(d)). The photocatalytic activity of the LiNa series also showed a close relationship with the degree of match between treatment temperature and melting point of the binary salt system. A series of characterization analyses, including XRD, FTIR, and SEM, were conducted to investigate the morphology and structure change of used catalysts. Based on the characterization results (Fig. S1†), it can be concluded that little morphology and structure change took place on LiK15 : 5 after the photocatalytic process.

3.3 Mechanism analysis

To investigate the light absorption ability of samples and calculate the bandgap width of the catalyst, UV-vis characterization was performed. All samples exhibited strong light absorption in the range of 220–450 nm (Fig. 7(a) and (b)). After treatment with molten salt, carbon nitride exhibited a red-

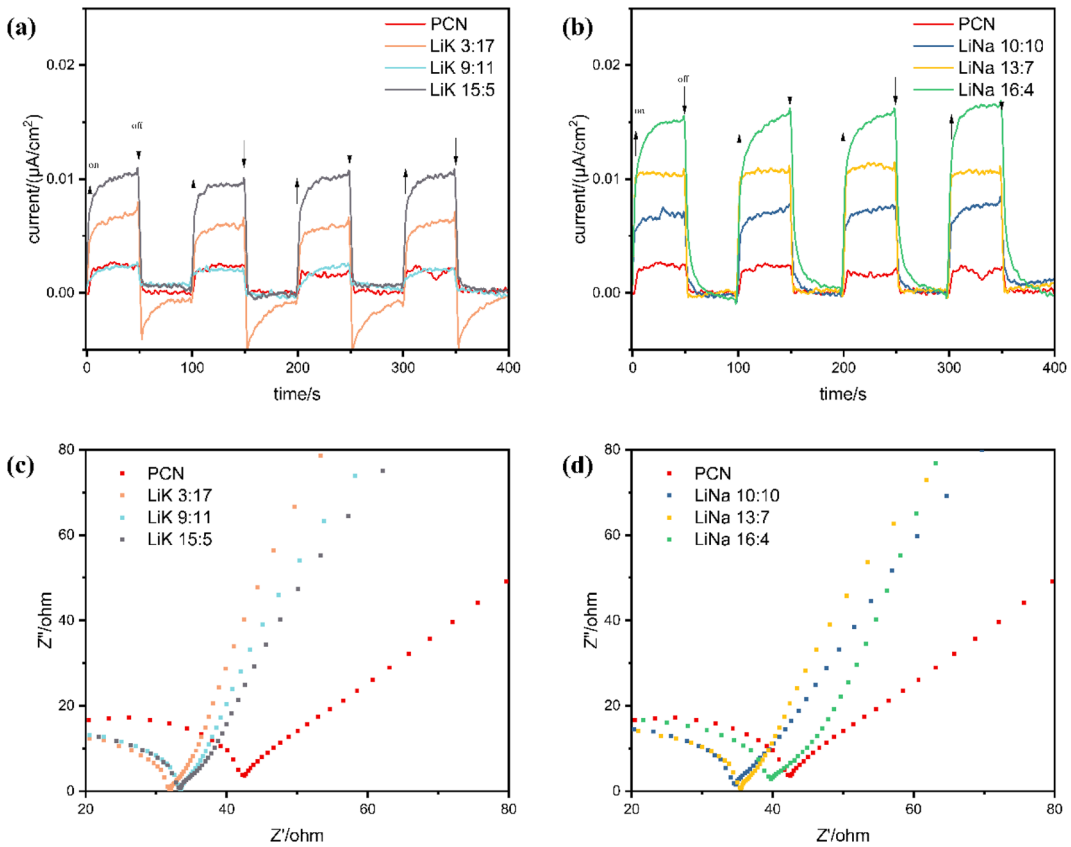

Fig. 8 (a and b) Transient photocurrent response, and (c and d) electrochemical impedance spectra (EIS) of PCN and CCN.

shifted edge wavelength and increased absorption of visible light, covering almost the entire ultraviolet-visible waveband.

Mott–Schottky (MS) plots of PCN and alkali-metal-doped crystalline g-C_3N_4 with an enriched cyano group are shown in Fig. 7(c) and (d). The *f*-intercept of the linear segment of the MS curve represents the flat-band potential (V_{fb}) of the sample. The slopes of the MS curves for all ten samples were positive, indicating that they were all N-type semiconductors (Fig. 7(c) and (d)). Because the conduction band potential (E_{CB}) of N-type semiconductors is typically about 0.3 eV lower than V_{fb},[50] V_{fb} (*versus* NHE) can be calculated using the formula V_{fb} (*versus* NHE) = V_{fb} (*versus* Ag/AgCl) + E^{θ} (Ag/AgCl, *versus* NHE). The E_{CB} of each sample was then calculated. Finally, based on the bandgap width data calculated using the cutoff method, the valence band value of each sample was calculated and is shown in Fig. 7(e) and (f). The alkali-metal-doped CCN had a smaller bandgap width and stronger absorption of visible light than PCN, and the valence band edges were all shifted down to varying degrees.

By turning the light on and off, the efficiency of the separation and transfer of photogenerated carriers in a photocatalyst can be studied using the transient photocurrent response. The photocurrent intensities of the alkali metal-doped CCNs increased to varying degrees (Fig. 8(a) and (b)). Their photocurrent responses were much higher than those of PCN, revealing that a much larger electron density could be obtained after co-decoration with alkali metals and cyano groups. In addition, when the light was turned off, the decay rates of the photocurrents over LiK15 : 5 and LiNa16 : 4 were slower than those of the remaining three, indicating that the process of electron transfer was relatively longer and more complicated.[51]

Nyquist plots obtained through EIS are shown in Fig. 8(c) and (d). The radius of the semicircle in the high-frequency region is related to the charge transfer of the catalyst block; the smaller the radius, the smaller the charge resistance, the faster the charge transfer, and the lower the recombination of photogenerated carriers and holes.[52] Treatment with the three types of molten salts reduced the electrical resistance of CN, promoting the transfer of photogenerated carriers. However, the ranking of the radii did not match the sequence of photocatalytic activities of the LiK and LiNa series.

PL intensity reflects the combination of photogenerated electrons and holes. The PL intensity of the alkali-doped CCN with cyano groups was significantly reduced compared to that of PCN (Fig. 9(a)), indicating that the molten salt treatments effectively reduced the rates of recombination of electrons and holes. The PL intensity of LiK15 : 5 was lower than that of LiNa16 : 4, suggesting that treatment with low-melting-point molten salts is more favorable for the separation of photogenerated charges and holes.

To illustrate the differences in methane adsorption among the various catalysts, MA-TPD experiments were performed. The

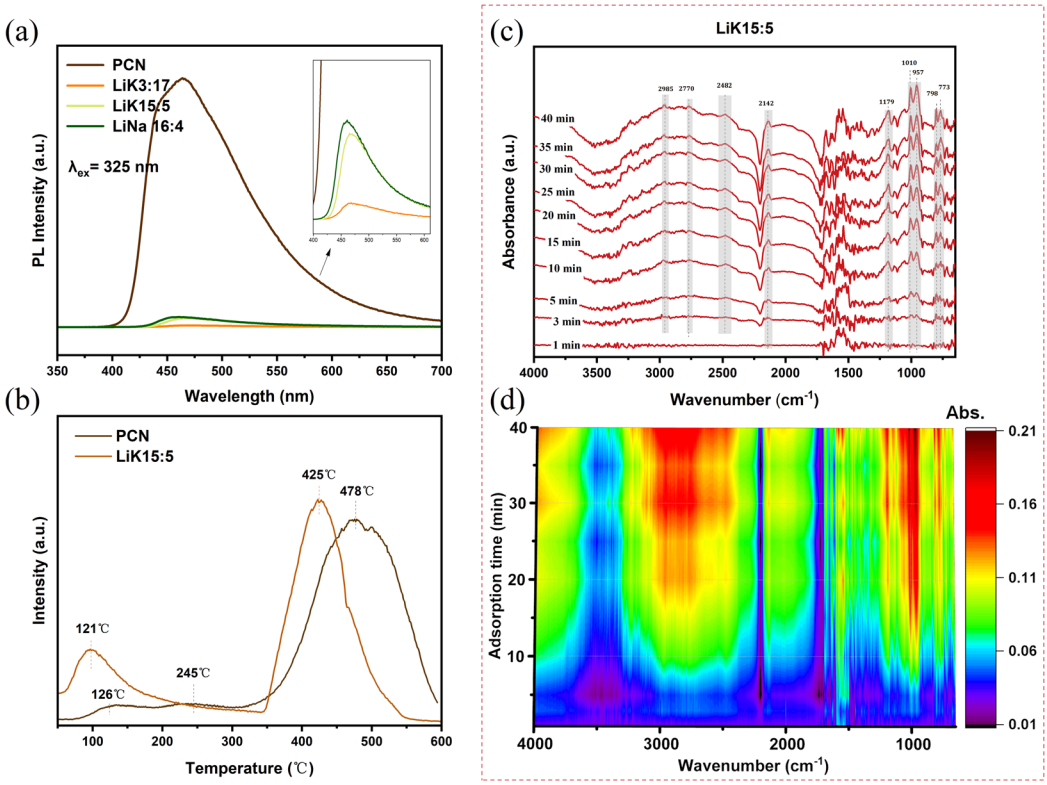

Fig. 9 (a) PL spectra, (b) MA-TPD spectra of PCN and CCN, (c) *in situ* DRIFTS spectra, and (d) DRIFTS intensity of MA adsorption process over LiK15 : 5 surface.

desorption peaks at 350–550 °C in Fig. 9(b) were attributed to chemisorption peaks on the catalyst, indicating strong interactions between the catalyst and methylamine. However, the desorption peaks at 100–300 °C were associated with weak acid sites or physically adsorbed methylamine.[53] The desorption peaks of PCN appeared at 126 °C, 245 °C and 478 °C, with the peaks at 126 °C and 245 °C being wider and flatter (Fig. 9(c)). In contrast, LiK15 : 5 showed two main peaks, at 121 °C and 425 °C, and the peaks shifted towards lower temperatures compared to PCN. The desorption peak area at 121 °C was bigger than that of PCN at 126 °C. This suggests that methylamine adsorbed on the surface of LiK15 : 5 was more active and easily participated in the reaction. Furthermore, the methylamine adsorption breakthrough experiments were performed for the adsorption capacity comparison of PCN and CCN. As shown in Fig. S2,† the breakthrough of methylamine on PCN took place when the methylamine was injected into the reactor and the balance of inlet and outlet was reached after 20 min adsorption. For LiNa13 : 7 and LiK15 : 5, the breakthroughs of methylamine took place when the methylamine was injected into the reactor for 5 min and the balance of inlet and outlet was reached after 40 min adsorption. In sum, the modification of alkali metal and cyano group on g-C_3N_4 strengthened the adsorption capacity of methylamine and enhanced the reaction activity of adsorbed methylamine.

To further elucidate the interaction between methylamine and the highly crystalline CN, *in situ* DRIFTS analysis was conducted. The infrared signals exhibited an increased adsorption time (Fig. 9(c) and (d)). The infrared signals exhibited two characteristic peaks at 2965 cm^{-1} and 2825 cm^{-1}, corresponding to the asymmetric and symmetric C–H stretching vibrations of the methyl (CH_3) group,[54] respectively. The broad vibrational peaks at 3454 cm^{-1} and 3565 cm^{-1} in the infrared spectra are indicative of the presence of NH_4^+ and NH_3 molecules adsorbed on the surface of the LiK15 : 5 sample. These results indicate that MA was easily adsorbed on the surface of LiK15 : 5, with a contribution of alkali ions in the interlayer or structure and the rich cyano groups in the structure of CCN.[53,55]

Fig. 10(a) and (b) show the DMPO–$^{\bullet}O_2^-$ and DMPO–$^{\bullet}OH$ EPR signals of PCN, LiK15 : 5, and LiNa13 : 7. None of the samples exhibited EPR signals in darkness, indicating that 5,5-dimethyl-1-pyrroline *N*-oxide (DMPO) had no paramagnetic center and that the samples could not generate radicals in the absence of light. Signals increased after light illumination, and signal intensity followed the ranked order LiK15 : 5 > LiNa13 : 7 > PCN, indicating that LiK15 : 5 had the highest concentration of photogenerated electrons in the localized π-conjugated structure.[56,57] Fig. 10(c) shows the TEMPO–h^+ EPR signals of PCN and LiK15 : 5 in the dark and under illumination. LiK15 : 5 exhibited a higher consumption of TEMPO (a spin trap for electrons/holes) than CN under illumination, suggesting that LiK15 : 5 can generate a larger number of photogenerated electrons, which may favor the generation of more superoxide radicals.[58] The EPR spectra under darkness

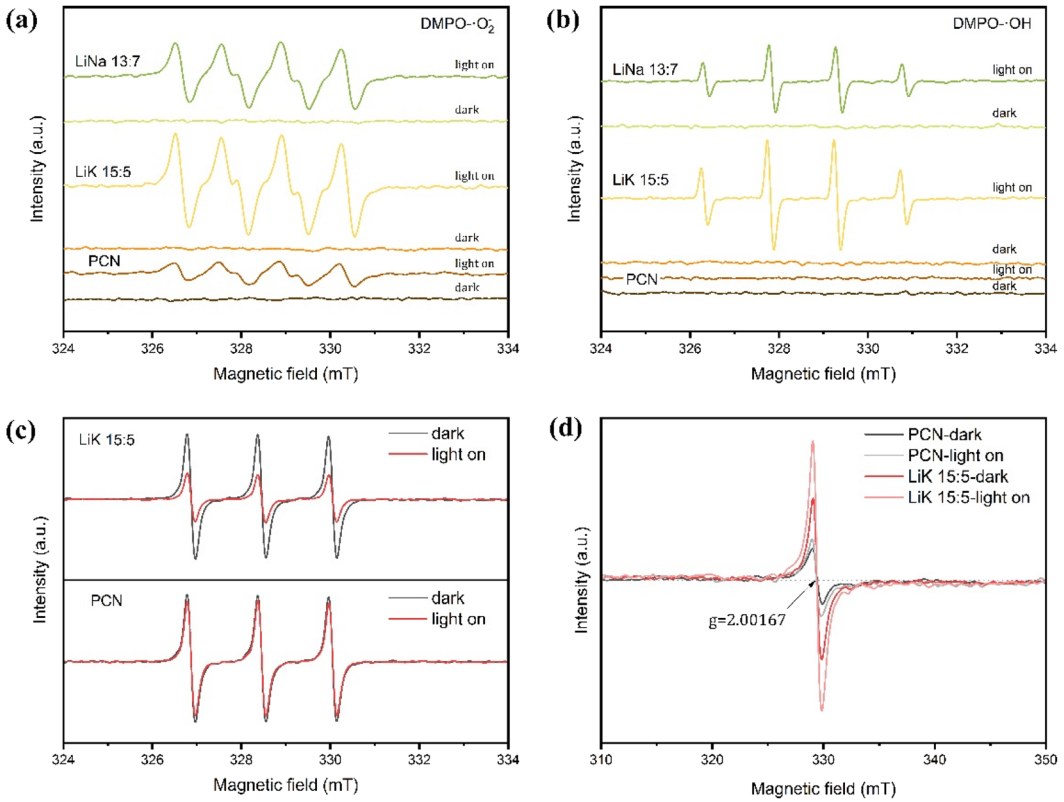

Fig. 10 (a) EPR signals of DMPO–$^{\cdot}O_2^-$ adducts; (b) the EPR signals of DMPO–$^{\cdot}OH$ adducts of PCN, LiK15 : 5, NaK15 : 5, and LiNa13 : 7 in darkness and under illumination; (c) EPR signals of TEMPO–h^+ adducts; and (d) EPR spectra of PCN and LiK15 : 5.

exhibited the same g ($g = 2.00167$), indicating the presence of the same paramagnetic species from unpaired electrons in the CN localized π-conjugated structure (Fig. 10(d)).[57] LiK15 : 5 exhibited a larger EPR signal intensity than PCN, suggesting more bulk phase defects and oxygen vacancies. Upon illumination, all samples exhibited increased EPR signals without exhibiting changes, indicating an intact π-conjugated structure and the generation of photoelectrons.[59]

4. Conclusions

In conclusion, this study demonstrated that calcining PCN in a molten salt environment with varying mass ratios generated CNN, and its performance as a noble-metal-free visible-light photocatalyst for the degradation of methylamine was studied. The optimized sample (LiK15 : 5) showed 10.2 times higher rates of degradation of methylamine than that of PCN. Furthermore, LiNa (13 : 7) showed a 4.9-fold increase compared with that of PCN. It was also demonstrated that crystalline g-C_3N_4 with a high surface area, good crystallinity, and co-doped cyano group and alkali metal, could be prepared under the melting point temperature of the binary salt. The mechanistic analysis revealed that the co-decoration of alkali metal and cyanide groups on crystalline g-C_3N_4 resulted in a much larger electron density, a stronger capacity for adsorption of methylamine, excellent photo-charge transfer efficiency, and generation of more superoxide radicals. Additionally, an increase in the heptazine ring ratio in CN in the melting environment resulted in better utilization of visible light. These findings highlight the effectiveness and feasibility of co-decoration of alkali metal and cyano groups on crystalline g-C_3N_4 and may inspire the development of more advanced photocatalysts for efficient visible-light photocatalytic degradation of methylamine.

Conflicts of interest

There are no conflicts to declare.

Acknowledgements

The authors acknowledge the financial support of this work from National Key Research and Development Program of China (2022YFC3702000), National Natural Science Foundation of China (NSFC-51978603), Hangzhou Qianjiang Distinguished Experts Project and the Program for Zhejiang Leading Team of S&T Innovation (Grant No. 2013TD07).

References

1 J. Fang, N. Yang, D. Cen, L. Shao and P. He, Odor compounds from different sources of landfill: characterization and source identification, *Waste Manage.*, 2012, **32**, 1401–1410.

2 C. Yang, C. Wang and C. Tseng, Methylamine removal using mixed bacterial strains in a continuous stirred tank reactor (CSTR) system, *Int. Biodeterior. Biodegrad.*, 2013, **85**, 583–586.
3 Y. Yi, X. Zhou, L. Xue and W. Wang, Air pollution: formation of brown, lighting-absorbing, secondary organic aerosols by reaction of hydroxyacetone and methylamine, *Environ. Chem. Lett.*, 2018, **16**, 1083–1088.
4 Z. Liu, M. Li, X. Wang, Y. Liang, Y. Jiang, J. Chen, J. Mu, Y. Zhu, H. Meng, L. Yang, K. Hou, Y. Wang and L. Xue, Large contributions of anthropogenic sources to amines in fine particles at a coastal area in northern China in winter, *Sci. Total Environ.*, 2022, **839**, 156281.
5 M. M. Kininge, S. K. Gujar, P. R. Gogate, A. Sharma, B. R. Mishra and D. Singh, Treatment of methylamine containing wastewater using combined processes based on ultrasound, *J. Water Process Eng.*, 2023, **51**, 103420.
6 K. M. Benjamin and P. E. Savage, Supercritical water oxidation of methylamine, *Ind. Eng. Chem. Res.*, 2005, **44**, 5318–5324.
7 S. H. Orojlou, B. Zargar and S. Rastegarzadeh, Metal oxide/TiO_2 nanocomposites as efficient adsorbents for relatively high temperature H_2S removal, *J. Nat. Gas Sci. Eng.*, 2018, **59**, 363–373.
8 R. C. Ruiz-Bastidas, G. Turnes, E. Palacio and L. S. Cadavid-Rodríguez, Natural Ecuadorian zeolite: an effective ammonia adsorbent to enhance methane production from swine waste, *Chemosphere*, 2023, **336**, 139098.
9 W. Liao, Z. Liang, Y. Yu, G. Li, Y. Li and T. An, Pollution profiles, removal performance and health risk reduction of malodorous volatile organic compounds emitted from municipal leachate treating process, *J. Cleaner Prod.*, 2021, **315**, 128141.
10 Y. Uesugi, H. Nagakawa and M. Nagata, Highly efficient photocatalytic degradation of hydrogen sulfide in the gas phase using anatase/TiO_2(B) nanotubes, *ACS Omega*, 2022, **7**, 11946–11955.
11 M. Chen, C. Zhang and H. He, Insights into designing photocatalysts for gaseous ammonia oxidation under visible light, *Environ. Sci. Technol.*, 2020, **54**, 10544–10550.
12 S. Lyu, W. Wu, R. Xiong, C. Yang, B. Sa, J. Zhang, Y. Hou and X. Wang, Carbon-rich carbon nitride nanocatalysts for H_2S selective oxidation, *J. Catal.*, 2022, **413**, 992–1004.
13 A. Kachina, S. Preis and J. Kallas, Gas-phase photocatalytic oxidation of dimethylamine: the reaction pathway and kinetics, *Int. J. Photoenergy*, 2007, **2007**, 79847.
14 S. Helali, F. Dappozze, S. Horikoshi, T. H. Bui, N. Perol and C. Guillard, Kinetics of the photocatalytic degradation of methylamine: influence of pH and UV-A/UV-B radiant fluxes, *J. Photochem. Photobiol., A*, 2013, **255**, 50–57.
15 X. Wang, K. Maeda, A. Thomas, K. Takanabe, G. Xin, J. M. Carlsson, K. Domen and M. Antonietti, A metal-free polymeric photocatalyst for hydrogen production from water under visible light, *Nat. Mater.*, 2009, **8**, 76–80.
16 Y. Yuan, T. Wang, H. Chen, S. M. Mahurin, H. Luo, G. M. Veith, Z. Yang and S. Dai, Ambient temperature graphitization based on mechanochemical synthesis, *Angew. Chem., Int. Ed.*, 2020, **59**, 21935–21939.
17 W. Ong, L. Tan, Y. H. Ng, S. Yong and S. Chai, Graphitic carbon nitride (g-C_3N_4)-based photocatalysts for artificial photosynthesis and environmental remediation: are we a step closer to achieving sustainability?, *Chem. Rev.*, 2016, **116**, 7159–7329.
18 X. Wu, S. Jiang, S. Song and C. Sun, Constructing effective photocatalytic purification system with P-introduced g-C_3N_4 for elimination of UO_2^{2+}, *Appl. Surf. Sci.*, 2018, **430**, 371–379.
19 M. Aksoy, S. E. Korkut and O. Metin, AuPt alloy nanoparticles supported on graphitic carbon nitride: in situ synthesis and superb catalytic performance in the light-assisted hydrolytic dehydrogenation of ammonia borane, *Appl. Surf. Sci.*, 2022, **602**, 154286.
20 X. Zhang, Y. Liu, L. Chen, Z. Li, Y. Qu, W. Wu and L. Jing, Porous two-dimension MnO_2-C_3N_4/titanium phosphate nanocomposites as efficient photocatalysts for CO oxidation and mechanisms, *Appl. Catal., B*, 2021, **282**, 119563.
21 Z. Cui, H. Yang and X. Zhao, Enhanced photocatalytic performance of g-C_3N_4/$Bi_4Ti_3O_{12}$ heterojunction nanocomposites, *Mater. Sci. Eng., B*, 2018, **229**, 160–172.
22 C. Ding, Q. Zhu, B. Yang, E. Petropoulos, L. Xue, Y. Feng, S. He and L. Yang, Efficient photocatalysis of tetracycline hydrochloride (TC-HCl) from pharmaceutical wastewater using AgCl/ZnO/g-C_3N_4 composite under visible light: process and mechanisms, *J. Environ. Sci.*, 2023, **126**, 249–262.
23 H. He, Z. Luo and C. Yu, Diatomite-anchored g-C_3N_4 nanosheets for selective removal of organic dyes, *J. Alloys Compd.*, 2020, **816**, 152652.
24 Y. Xu, C. Qiu, X. Fan, Y. Xiao, G. Zhang, K. Yu, H. Ju, X. Ling, Y. Zhu and C. Su, K^+-induced crystallization of polymeric carbon nitride to boost its photocatalytic activity for H_2 evolution and hydrogenation of alkenes, *Appl. Catal., B*, 2020, **268**, 118457.
25 W. An, X. Zhi, B. Zhai, P. Niu, S. Wang and L. Li, Crystallinity improvement of poly(heptazine imide) for high photocatalytic hydrogen evolution, *Scr. Mater.*, 2022, **221**, 114992.
26 Y. Xu, X. He, H. Zhong, D. J. Singh, L. Zhang and R. Wang, Solid salt confinement effect: an effective strategy to fabricate high crystalline polymer carbon nitride for enhanced photocatalytic hydrogen evolution, *Appl. Catal., B*, 2019, **246**, 349–355.
27 Y. Wang, X. Zhang, Y. Liu, Y. Zhao, C. Xie, Y. Song and P. Yang, Crystallinity and phase controlling of g-C_3N_4/CdS heterostructures towards high efficient photocatalytic H_2 generation, *Int. J. Hydrogen Energy*, 2019, **44**, 30151–30159.
28 Y. Guo, J. Li, Y. Yuan, L. Li, M. Zhang, C. Zhou and Z. Lin, A rapid microwave-assisted thermolysis route to highly crystalline carbon nitrides for efficient hydrogen generation, *Angew. Chem., Int. Ed.*, 2016, **55**, 14693–14697.
29 L. Tan, C. Nie, Z. Ao, H. Sun, T. An and S. Wang, Novel two-dimensional crystalline carbon nitrides beyond g-C_3N_4: structure and applications, *J. Mater. Chem. A*, 2021, **9**, 17–33.

30 J. Wang, Y. Xia, H. Zhao, G. Wang, L. Xiang, J. Xu and S. Komarneni, Oxygen defects-mediated Z-scheme charge separation in g-C_3N_4/ZnO photocatalysts for enhanced visible-light degradation of 4-chlorophenol and hydrogen evolution, *Appl. Catal., B*, 2017, **206**, 406–416.

31 C. Zhu, X. Luo, C. Liu, Y. Wang, X. Chen, Y. Wang, Q. Hu, X. Wu and B. Liu, Defect-rich ultrathin poly-heptazine-imide-framework nanosheets with alkali-ion doping for photocatalytic solar hydrogen and selective benzylamine oxidation, *Nano Res.*, 2022, **15**, 8760–8770.

32 D. Zhang, Y. Guo and Z. Zhao, Porous defect-modified graphitic carbon nitride via a facile one-step approach with significantly enhanced photocatalytic hydrogen evolution under visible light irradiation, *Appl. Catal., B*, 2018, **226**, 1–9.

33 Q. You, C. Zhang, M. Cao, B. Wang, J. Huang, Y. Wang, S. Deng and G. Yu, Defects controlling, elements doping, and crystallinity improving triple-strategy modified carbon nitride for efficient photocatalytic diclofenac degradation and H_2O_2 production, *Appl. Catal., B*, 2023, **321**, 121941.

34 G. Zhang, G. Li, T. Heil, S. Zafeiratos, F. Lai, A. Savateev, M. Antonietti and X. Wang, Tailoring the grain boundary chemistry of polymeric carbon nitride for enhanced solar hydrogen production and CO_2 reduction, *Angew. Chem., Int. Ed.*, 2019, **58**, 3433–3437.

35 L. Lin, W. Ren, C. Wang, A. M. Asiri, J. Zhang and X. Wang, Crystalline carbon nitride semiconductors prepared at different temperatures for photocatalytic hydrogen production, *Appl. Catal., B*, 2018, **231**, 234–241.

36 T. Huang, R. Wang, J. Zhang, J. Wang, H. Ge, J. Ren and Z. Zheng, Cyano group modified graphitic carbon nitride supported Ru nanoparticles for enhanced CO_2 methanation, *Chem. Eng. J.*, 2023, **467**, 143469.

37 X. Zhong, Y. Zhu, M. Jiang, Q. Sun and J. Yao, Dual defective K-doping and cyano group sites on carbon nitride nanotubes for improved hydrogen photo-production, *Energy Fuels*, 2023, **37**, 5448–5456.

38 C. W. Bale, E. Bélisle, P. Chartrand, S. A. Decterov, G. Eriksson, A. E. Gheribi, K. Hack, I.-H. Jung, Y.-B. Kang, J. Melançon, A. D. Pelton, S. Petersen, C. Robelin, J. Sangster, P. Spencer and M.-A. Van Ende, FactSage thermochemical software and databases, 2010–2016, *Calphad*, 2016, **54**, 35–53.

39 Z. Lin, X. Tong, W. Shen, J.-C. Roux and H. Xi, Humidity impact on photo-catalytic degradation: adsorption behavior simulations and catalytic reaction mechanisms for main gaseous pollutants in papermaking industry, *J. Cleaner Prod.*, 2020, **244**, 118863.

40 Y. Zhu, T. Wang, T. Xu, Y. Li and C. Wang, Size effect of Pt co-catalyst on photocatalytic efficiency of g-C_3N_4 for hydrogen evolution, *Appl. Surf. Sci.*, 2019, **464**, 36–42.

41 Z. Chen, A. Savateev, S. Pronkin, V. Papaefthimiou, C. Wolff, M. G. Willinger, E. Willinger, D. Neher, M. Antonietti and D. Dontsova, "The easier the better" preparation of efficient photocatalysts-metastable poly(heptazine imide) salts, *Adv. Mater.*, 2017, **29**, 1700555.

42 L. Lin, H. Ou, Y. Zhang and X. Wang, Tri-*s*-triazine-based crystalline graphitic carbon nitrides for highly efficient hydrogen evolution photocatalysis, *ACS Catal.*, 2016, **6**, 3921–3931.

43 I. Y. Kim, S. Kim, X. Jin, S. Premkumar, G. Chandra, N. Lee, G. P. Mane, S. Hwang, S. Umapathy and A. Vinu, Ordered mesoporous C_3N_5 with a combined triazole and triazine framework and its graphene hybrids for the oxygen reduction reaction (ORR), *Angew. Chem., Int. Ed.*, 2018, **130**, 17381–17386.

44 D. Burmeister, J. Müller, J. Plaickner, Z. Kochovski, E. J. W. List-Kratochvil and M. J. Bojdys, Size effects of the anions in the ionothermal synthesis of carbon nitride materials, *Chem.–Eur. J.*, 2022, **28**, e202200705.

45 M. Arumugam, M. Tahir and P. Praserthdam, Effect of nonmetals (B, O, P, and S) doped with porous g-C_3N_4 for improved electron transfer towards photocatalytic CO_2 reduction with water into CH_4, *Chemosphere*, 2022, **286**, 131765.

46 C. Yu, H. He, W. Zhou, Z. Liu and L. Wei, Novel rugby-ball-like $Zn_3(PO_4)_2$@C_3N_4 photocatalyst with highly enhanced visible-light photocatalytic performance, *Sep. Purif. Technol.*, 2019, **217**, 137–146.

47 B. Chen, W. Lu, P. Xu and K. Yao, Potassium poly(heptazine imide) coupled with Ti_3C_2 MXene-derived TiO_2 as a composite photocatalyst for efficient pollutant degradation, *ACS Omega*, 2023, **8**, 11397–11405.

48 H. He, J. Li, C. Yu and Z. Luo, Surface decoration of microdisk-like g-C_3N_4/diatomite with Ag/AgCl nanoparticles for application in Cr(VI) reduction, *Sustainable Mater. Technol.*, 2019, **22**, e00127.

49 S. Cao, J. Low, J. Yu and M. Jaroniec, Polymeric photocatalysts based on graphitic carbon nitride, *Adv. Mater.*, 2015, **27**, 2150–2176.

50 Y. Gao, J. Duan, X. Zhai, F. Guan, X. Wang, J. Zhang and B. Hou, Photocatalytic degradation and antibacterial properties of Fe^{3+}-doped alkalized carbon nitride, *Nanomaterials*, 2020, **10**, 1751.

51 J. Zhuang, S. Weng, W. Dai, P. Liu and Q. Liu, Effects of interface defects on charge transfer and photoinduced properties of TiO_2 bilayer films, *J. Phys. Chem. C*, 2012, **116**, 25354–25361.

52 N. M. Ghazy, E. A. Ghaith, Y. G. Abou El-Reash, R. R. Zaky, W. M. Abou El-Maaty and F. S. Awad, Enhanced performance of hydroxyl and cyano group functionalized graphitic carbon nitride for efficient removal of crystal violet and methylene blue from wastewater, *RSC Adv.*, 2022, **12**, 35587–35597.

53 C. Fernandez-Ruiz, J. Bedia, J. M. Grau, A. C. Romero, D. Rodríguez, J. J. Rodríguez and L. M. Gómez-Sainero, Promoting light hydrocarbons yield by catalytic hydrodechlorination of residual chloromethanes using palladium supported on zeolite catalysts, *Catalysts*, 2020, **10**, 199.

54 R. Tian, J. Lu, Z. Xu, W. Zhang, J. Liu, L. Wang, Y. Xie, Y. Zhao, X. Cao and Y. Luo, Unraveling the synergistic reaction and the deactivation mechanism for the catalytic degradation of double components of sulfur-containing

VOCs over ZSM-5-based materials, *Environ. Sci. Technol.*, 2023, **57**, 1443–1455.

55 P. Wang, Z. Shen, Y. Xia, H. Wang, L. Zheng, W. Xi and S. Zhan, Atomic insights for optimum and excess doping in photocatalysis: A case study of few-layer Cu-$ZnIn_2S_4Z$, *Adv. Funct. Mater.*, 2019, **29**, 1807013.

56 J. Li, X. Dong, Y. Sun, G. Jiang, Y. Chu, S. C. Lee and F. Dong, Tailoring the rate-determining step in photocatalysis via localized excess electrons for efficient and safe air cleaning, *Appl. Catal., B*, 2018, **239**, 187–195.

57 P. Xia, B. Cheng, J. Jiang and H. Tang, Localized π-conjugated structure and EPR investigation of g-C_3N_4 photocatalyst, *Appl. Surf. Sci.*, 2019, **487**, 335–342.

58 L. Shi, G. Liu, Y. Zhang and Z. Yang, Na, O co-doping and cyano groups synergistically adjust the band structure of g-C_3N_4 for improving photocatalytic oxygen evolution, *Mater. Res. Bull.*, 2023, **167**, 112423.

59 W. Ho, Z. Zhang, W. Lin, S. Huang, X. Zhang, X. Wang and Y. Huang, Copolymerization with 2,4,6-triaminopyrimidine for the rolling-up the layer structure, tunable electronic properties, and photocatalysis of g-C_3N_4, *ACS Appl. Mater. Interfaces*, 2015, **7**, 5497–5505.